Enhanced Condensation on Lubricant-Impregnated Nanotextured Surfaces

Sushant Anand, Adam T. Paxson, Rajeev Dhiman, J. David Smith, and Kripa K. Varanasi*

Department of Mechanical Engineering, Massachusetts Institute of Technology, 77 Massachusetts Avenue, Cambridge, Massachusetts 02139, United States

ABSTRACT

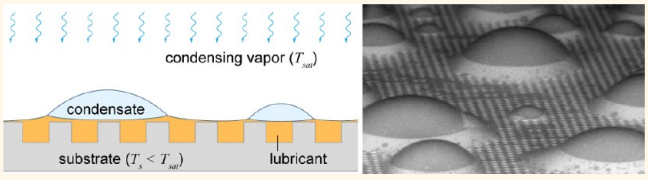

Nanotextured superhydrophobic surfaces have received significant attention due to their ability to easily shed liquid drops. However, water droplets have been shown to condense within the textures of superhydrophobic surfaces, impale the vapor pockets, and strongly pin to the surface. This results in poor droplet mobility and degrades condensation performance. In this paper, we show that pinning of condensate droplets can be drastically reduced by designing a hierarchical micro-nanoscale texture on a surface and impregnating it with an appropriate lubricant. The choice of lubricant must take into account the surface energies of all phases present. A lubricant will cloak the condensate and inhibit growth if the spreading coefficient is positive. If the lubricant does not fully wet the solid, we show how condensate—solid pinning can be reduced by proper implementation of nanotexture. On such a surface, condensate droplets as small as 100 μm become highly mobile and move continuously at speeds that are several orders of magnitude higher than those on identically textured superhydrophobic surfaces. This remarkable mobility produces a continuous sweeping effect that clears the surface for fresh nucleation and results in enhanced condensation.

KEYWORDS: dropwise condensation · slippery surfaces · droplet mobility · liquid-impregnated surfaces · nanotextured surfaces

Condensation of vapor is ubiquitous in many industrial processes, such as power generation, desalination, water harvesting, air conditioning, thermal management, and transportation, and enhancing the heat transfer during condensation can have a significant impact on the overall energy efficiency in these applications.[1−4] While the condensing surface can be rigid,[5−7] soft,[8,9] or liquid,[10−12] the condensate usually forms either as a film or as discrete drops depending on the wettability of the surface: the lower the wettability, the greater the likelihood of drop formation.[5,6,13,14] Numerous studies have shown that heat transfer during the dropwise mode of condensation is significantly higher than the filmwise mode because in the latter case the condensate film acts as a major thermal barrier.[1,2] In contrast, condensate drops in the dropwise mode can be continuously shed to allow for renewed nucleation and growth of droplets.[1−3,15] This has inspired various approaches to realize dropwise condensation.[3]

Recently, there has been significant interest in developing superhydrophobic surfaces for promoting dropwise condensation.[6,16−25] Such surfaces combine microscopic roughness with hydrophobicity in order to attain extreme non-wetting properties with water droplets, which rest atop roughness features with vapor trapped underneath (Cassie state).[26] Since Cassie droplets have minimal contact with the surface, they can be easily shed.[26] However, under condensation, many natural and synthetic superhydrophobic surfaces display poor drop mobility due to nucleation of droplets within texture features (Figure 1a, b) that ultimately results in sticky, Wenzel droplets (Figure 1c; see Video S1).[6,19,27−30] To overcome these limitations, hybrid hydrophobic—hydrophilic surfaces that promote Cassie condensation[6,31] and micro-nano textures that promote coalescence-induced self-propelled dropwise condensation have been developed.[17,18] Though promising, these approaches require surface textures with intricate designs and morphologies[32−34] that are vulnerable to damage and defects.

Here we present an alternate approach to promote dropwise condensation in which the condensing surface is microscopically textured and impregnated with a lubricating liquid immiscible with the condensed liquid (Figure 1d). Such surfaces have recently been shown to display low contact angle hysteresis,[35,36] self-cleaning,[36,37] self-healing by wicking upon damage, repellency to variety of liquids,[37] and remarkable anti-icing properties.[38] Furthermore, the shedding velocity of droplets from such surfaces has been shown to be inversely dependent upon viscosity.[39] In this paper we show that by appropriately choosing the lubricant

* Address correspondence to varanasi@mit.edu.

Received for review August 23, 2012 and accepted October 2, 2012.

Published online October 02, 2012
10.1021/nn303867y

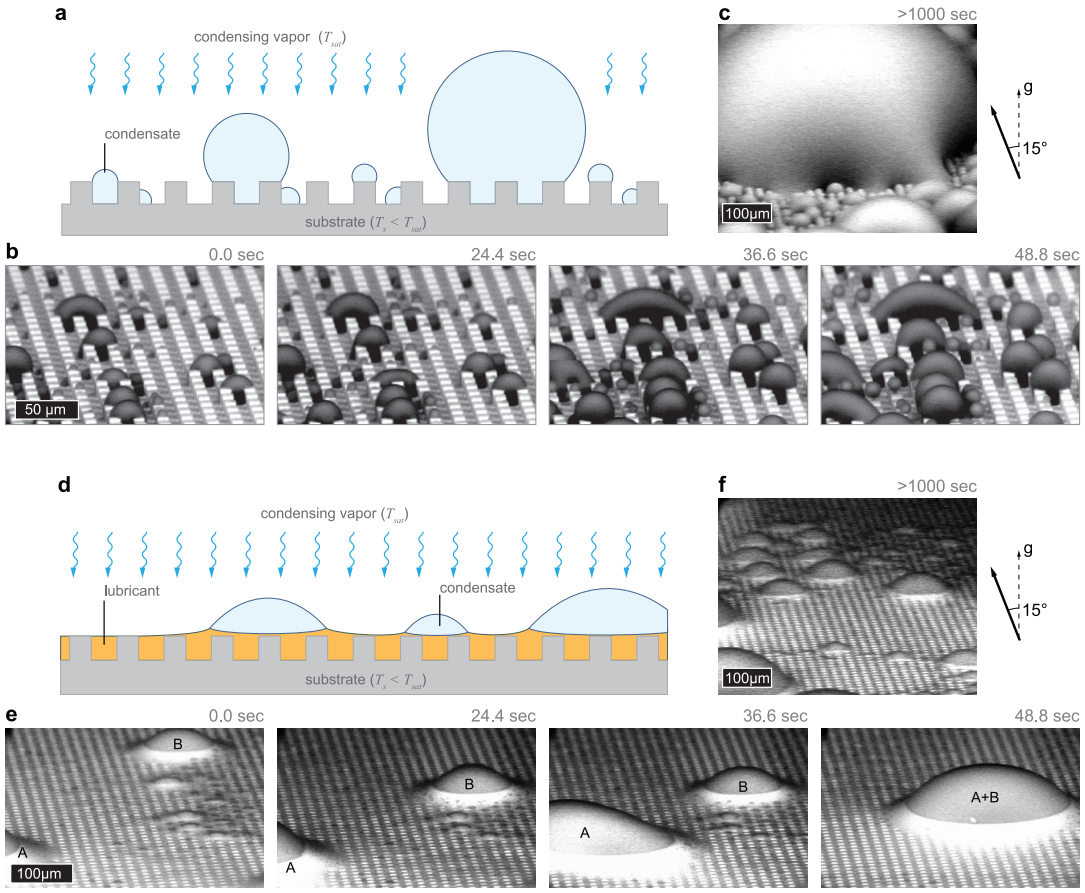

Figure 1. Comparison of condensation of water vapor on superhydrophobic and lubricant-impregnated surfaces with identical texture. (a) Schematic of condensation on a superhydrophobic surface showing the formation of droplets throughout the texture. (b) ESEM image sequence of condensation on a hierarchical superhydrophobic surface comprising nanotextured micropost arrays (see Figure 3e). Droplets randomly nucleate on the top and within the texture features, grow and coalesce, and eventually (t > 1000 s) form (c) a large Wenzel droplet that is highly pinned. (d) Schematic of condensation on a lubricant-impregnated surface showing that droplets remain afloat on a lubricant film without impaling into the surface texture. (e) ESEM image sequence showing growth and motion of microscopic droplets on a nanotextured micropost array surface impregnated with ionic liquid. Drop B moves against gravity and coalesces with another randomly moving droplet, A, at 48.8 s, thereby clearing the surface for further nucleation. (f) ESEM image shows even after long time (>1000 s) small droplets remain mobile and clear the surface for further nucleation. The ESEM experiments were conducted under identical conditions (pressure 1000 Pa, substrate temperature ~4.5 °C, beam voltage 25 kV, and beam current 1.7 nA; the surfaces were titled by 15° to the vertical). See Video S1 for the complete sequence and comparison of condensation on the two surfaces.

and designing the geometry and chemistry of the texture, enhanced condensation can be achieved (Figure 1e, f). We demonstrate that condensate droplets of water as small as 100 μm become mobile on such surfaces, continually sweeping them and creating fresh areas for further nucleation (Figure 1e, f; see Video S1). We capture the growth and shedding of the condensing droplets through direct imaging in an environmental scanning electron microscope (ESEM) as well as in a controlled-environment condensation apparatus. We also investigate the effect of surface texture and the interplay of the interfacial energies of the lubricant, textured surface, and droplets in order to facilitate the design of such surfaces for enhanced condensation.

RESULTS AND DISCUSSION

We begin by describing the conditions necessary to impregnate a lubricating liquid into a textured surface and subsequently prevent its possible displacement out of the texture once condensate droplets start to form. Preventing lubricant displacement is important to avoid droplets from impaling the texture and becoming stuck.[36] For simplicity, we refer to the lubricant as oil and condensate droplets as water. It has been shown that an oil will impregnate a textured surface if $\theta_{os(v)} \leq \theta_c$, where $\theta_{os(v)}$ is the contact angle of oil (subscript "o") on the smooth solid (subscript "s") in the presence of vapor (subscript "v"), and θ_c is the critical contact angle for impregnation, given by $\theta_c = \cos^{-1}[(1 -)/(r - \phi)]$.[36] Here, ϕ is the fraction of the projected area of the textured surface that is occupied by a solid and r is the ratio of total surface area of the textured surface to its projected area.[36] For example, in the case of microposts, $\phi = a^2/(a + b)^2$ and $r = 1 + 4ah/(a + b)^2$, where a is the post width, b is the edge-to-edge spacing between posts, and h is the post height.

In the special case of $\theta_{os(v)} = 0$, the entire texture is covered with oil. When this condition is not met, portions of the texture are left uncovered above locations where the local contact angle of oil equals $\theta_{os(v)}$.[35,36] Once water droplets begin to form on the textured surface, the lubricant forms an annular "wetting ridge" around the condensed droplet (depicted by bright areas in Figure 1f) to satisfy the force balance between the interfacial tensions. The condensate drops can displace the oil from the texture unless $\theta_{os(w)} \leq \theta_c$, where $\theta_{os(w)}$ is the contact angle of oil on the smooth solid in the presence of water (subscript "w").[36,39] Again, if $\theta_{os(w)} = 0$, the entire texture underneath the water droplets would be covered with oil, whereas when this condition is not met, portions of the texture will remain uncovered and exposed to water. In addition to the above two conditions, a less obvious task in designing lubricant-impregnated surfaces is to consider the possibility of cloaking (or encapsulation) of water droplets by the impregnated oil.[39] This can happen when the spreading coefficient of oil on water in the presence of vapor is positive, *i.e.*, $S_{ow(v)} > 0$, where $S_{ow(v)} = \gamma_{wv} - \gamma_{ov} - \gamma_{ow}$, and γ_{ij} is the interfacial tension between the phases i and j.[40,41] It is important to consider cloaking because it may prevent condensate growth, accelerate oil depletion from the texture, and contaminate the droplets. Conversely, the condensate may completely spread on oil if $S_{wo(v)} > 0$, where $S_{wo(v)} = \gamma_{ov} - \gamma_{wv} - \gamma_{ow}$, leading to filmwise condensation. This scenario may occur during condensation of low-surface energy liquids such as refrigerants and organic liquids. Therefore, in order to avoid cloaking and promote dropwise condensation, $S_{ow(v)} < 0$ and $S_{wo(v)} < 0$.

On the basis of the above considerations, we chose two different lubricants for our study: a fluorinated oil (Krytox-1506, DuPont) and an ionic liquid (1-butyl-3-methylimidazolium bis(trifluoromethylsulfonyl)imide, $[BMIm^+][Tf_2N^-]$), which we will refer to as BMIm for simplicity. Water was used as the condensing fluid. The condensing surfaces were well-defined cubical microposts of silicon (a = 10 μm, b = 10 μm, and h = 10 μm) fabricated by standard photolithography. A low-energy silane (octadecyltrichlorosilane, OTS) was coated on the textured surfaces using solution-based deposition in order to render them hydrophobic (advancing water contact angle = 110° ± 4°) and preferentially wet by the lubricants. Lubricants were impregnated into the textured surfaces by dipping them into a bath of lubricant and then withdrawing at controlled rates using a dip coater.[42] This procedure ensured high reproducibility and no excess impregnation of the lubricant. Two different types of experimental approaches were used to study the condensation phenomena: at the microscale, an ESEM was used at low subcooling conditions to analyze the early stages of condensation, whereas at the macroscale, a controlled-environment condensation rig connected to a 20 kW boiler was used to examine droplet shedding and departure diameters. Contact angles of both lubricants on smooth OTS-coated silicon surfaces were measured in the presence of air as well as water. In addition, the interfacial tensions of lubricants in the presence of water were measured using the pendant drop method.[43] All of the above parameters, along with the relevant physical properties of the lubricants, are listed in Table 1, from which several points are noteworthy. First, $S_{wo(v)} < 0$ for both lubricants, implying that water vapor would condense as droplets in both cases. Second, $S_{ow(v)} < 0$ for BMIm, but for Krytox, $S_{ow(v)} > 0$, indicating that Krytox would cloak the condensed water droplets, whereas cloaking would not be expected in the case of BMIm. Third, $\theta_{os(v)}$ is non-zero but less than θ_c for both Krytox and BMIm, indicating that the micropost tops will be left uncovered after impregnation. Fourth, since $\theta_{os(w)} < \theta_c$ for both Krytox and BMIm, water droplets are expected to remain atop rather than impale into the texture. Finally, both lubricants have extremely low vapor pressure, especially BMIm, which mitigates the concern of lubricant loss through evaporation.

We first analyze the effect of lubricant cloaking on the early stages of condensation using ESEM (Video S2). The experiments were conducted at low subcoolings (substrate temperature $T_s \approx 3.6$ °C, saturation temperature T_{sat} = 3.8 °C at P = 800 Pa) so that the condensation rate was not too high to be captured in ESEM (imaging rate 0.5 fps). These results are shown in Figure 2, which reveals that the droplet growth patterns obtained with the two lubricants are substantially different. On the Krytox-impregnated surface (Figure 2a, $S_{ow(v)} > 0$), condensation is significantly inhibited as the droplets (black spots in the images) grow or coalesce little compared with those on the BMIm-impregnated surface (Figure 2c, $S_{ow(v)} < 0$). Furthermore, droplets attain a barrel shape (time t = 111.9 s) on the BMIm-impregnated surface as the dry hydrophobic post tops pin (Figure 2d) and confine droplets during the growth process. We calculated droplet coverage in each case by measuring the fraction of the total area of the images that was occupied by droplets. These results are given in Figure 2e, which clearly shows that the coverage of water droplets is both much faster and larger on the surface impregnated with BMIm compared to the one impregnated with Krytox. The suppression of droplet growth in the case of Krytox-impregnated surface becomes more clear when we plot the number density of droplets with time and compare it with the BMIm-impregnated surface. These measurements are shown in Figure 2f and reveal that the droplet number density first increases sharply due to nucleation and

then decreases due to coalescence in the case of the BMIm-impregnated surface. Comparatively, the droplet number density on the Krytox-impregnated surface increases weakly, showing that droplet growth was significantly inhibited in this case. Furthermore, the condensed droplets on the Krytox-impregnated surface could not be evaporated even under high superheat conditions ($T_s - T_{sat}$ = 20 °C, Video S3). The above findings suggest that cloaking occurred during condensation on the Krytox-impregnated surface (Figure 2b) and did not occur on the BMIm-impregnated surface (Figure 2d), as predicted by their respective spreading coefficients (Table 1). It should be noted that cloaked droplets can grow through coalescence by draining the lubricant film between them,[46] which could be achieved through droplet confinement (*e.g.*, within textures) while increasing their number density using higher supersaturation.

Next, we analyze the effect of surface texture on the mobility of condensed droplets using ESEM. Figure 3a shows condensate drops (indicated by A–F) growing

TABLE 1. Properties of Krytox and Ionic Liquid at Room Temperature

parameter	units	Krytox	BMIm
γ_{ov}[44]	mN/m	17	34
γ_{ow}[a]	mN/m	49	13
$S_{ow(v)}$[a]	mN/m	6	−5
$S_{wo(v)}$[a]	mN/m	−104	−21
$\theta_{os(v)}$	deg	28 ± 4	64 ± 4
$\theta_{os(w)}$	deg	28 ± 4	37 ± 4
θ_c	deg	65	65
density[45]	kg/m^3	1860	1430
dynamic viscosity[45]	Pa·s	0.116	0.032
vapor pressure	mmHg	$<4 \times 10^{-7}$	$<10^{-12}$

[a] See Supporting Information.

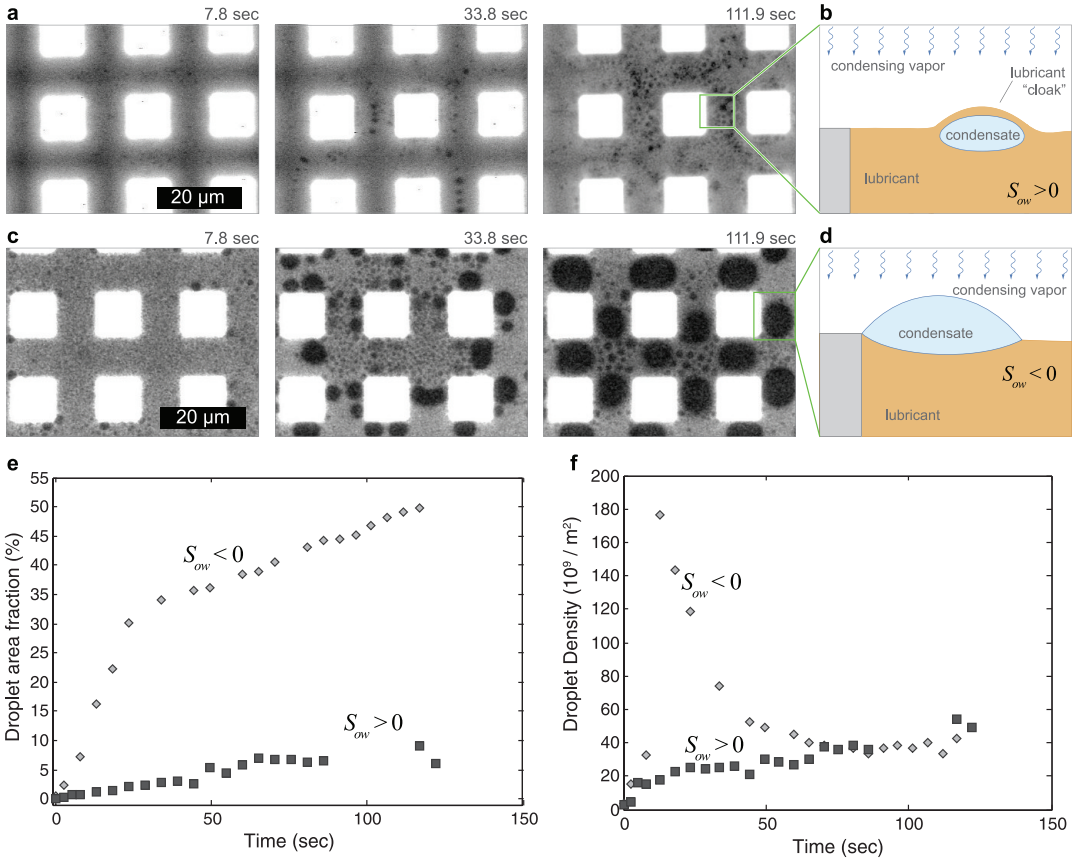

Figure 2. (a) ESEM image sequence of condensation on a micropost surface impregnated with Krytox that has a positive spreading coefficient on water ($S_{ow} > 0$). Condensation is inhibited as Krytox cloaks the condensed droplets. (b) Illustration of cloaked condensate droplet depicting the thin film of condensate that spreads on the droplet. (c) ESEM image sequence of condensation on micropost surface impregnated with BMIm that has a negative spreading coefficient with water ($S_{ow} < 0$). (d) Illustration of uncloaked condensate droplet depicting the three phase contact line of the water–vapor, water–lubricant, and lubricant–vapor interfaces on one end and pinning of the droplet at the dry post tops at the other end. (e) Plot comparing variation of surface area fraction covered by condensed water droplets *versus* time on surfaces impregnated with Krytox ($S_{ow} > 0$, solid squares) and BMIm ($S_{ow} < 0$, open diamonds). (f) Plot comparing number of water droplets per unit area *versus* time on surfaces impregnated with Krytox (solid squares) and BMIm (open diamonds). The ESEM experiments were conducted under identical conditions (pressure 800 Pa, substrate temperature ~3.6 °C, beam voltage 25 kV, and beam current 1.7 nA). In the analysis, t = 0 s is defined as the first frame in which water drops can be identified.

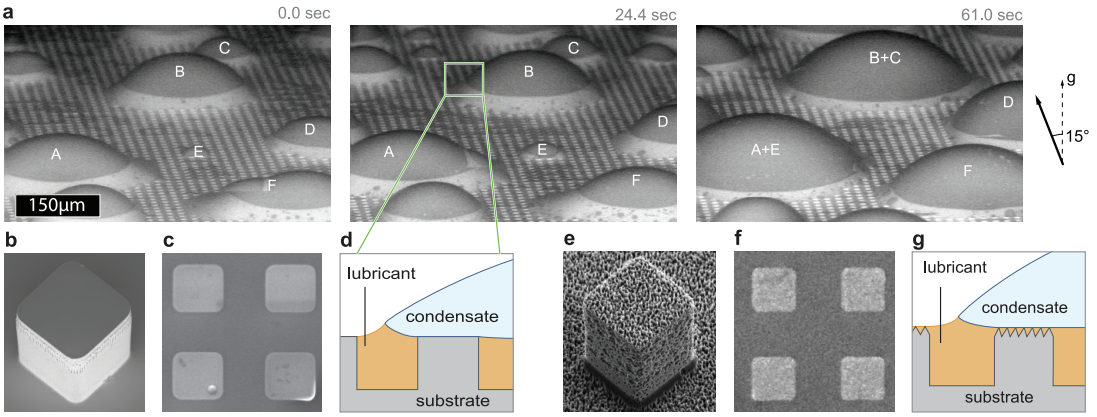

Figure 3. (a) Image sequence showing growth of water droplets during condensation on micropost surface impregnated with BMIm. The images show that large droplets appear to grow and coalesce while still remaining at the same location; there is no significant movement of drops. Also evident is the water–lubricant–vapor contact line that is pulled above the substrate, forming a wetting ridge. (b) SEM of a single smooth micropost. (c) Top-view SEM of smooth microposts impregnated with BMIm. A stable BMIm droplet can be seen on the surface, indicating that the post tops are dry. (d) Schematic of a droplet on a textured surface that has been impregnated with a liquid for which $\theta_{os(w)} > 0$, depicting the exposed post tops beneath the water droplet and the pulled-up water–lubricant–vapor contact line. (e) SEM of a single micropost with etched nanograss structures. (f) SEM of impregnated surface with nanotextured microposts. (g) Schematic of a droplet on the nanograss micropost surfaces that has been impregnated with a lubricant. The nanograss allows for the lubricant to impregnate the post tops, resulting in reduced condensate–solid pinned fraction. The ESEM experiments were conducted under identical conditions (pressure 1400 Pa, substrate temperature ~7.7 °C, beam voltage 25 kV, and beam current 1.7 nA). See Video S4 for more details.

and coalescing on a micropost surface impregnated with BMIm. Although the drops grow, either by coalescence (droplets A and E, and B and C) or by direct condensation (droplets D and F), they remain largely immobile. This suggests that the drops were pinned to the texture probably at the post tops (Figure 3d), which is plausible since both $\theta_{os(v)}$ and $\theta_{os(w)}$ were non-zero in the case of BMIm. Also, the presence of a small drop of BMIm instead of a thin film on the post top (Figure 3c), along with the formation of barrel-shaped drops between the posts (Figure 2c), indicates that the post tops were uncovered by BMIm. This also explains the preferential condensation within the pillar gaps (Figure 2a and c) since compared with the uncovered and hydrophobic post tops, the lubricants have higher surface energy and thus lower nucleation energy barrier. To reduce pinning and enhance drop mobility, we added a smaller level of roughness by etching nanograss on the posts (Figure 3e) and impregnated it with BMIm. The additional capillary force imparted by the nanograss stabilizes BMIm even on post tops (Figure 3f), thereby reducing the uncovered solid where condensing drops could pin (Figure 3g). Consequently, when we condensed water vapor on this surface, we observed a dramatic increase in droplet mobility (Figure 1e): drops as small as 100 μm move rapidly across the surface (see Video S4). Therefore, hierarchical nano-microtextures impregnated with lubricant can significantly enhance droplet mobility by reducing the solid fraction available for contact line pinning, as depicted in Figure 3g.

Finally, we investigate the macroscopic behavior of condensed droplets on a BMIm-impregnated surface and compare it with a superhydrophobic surface having the same texture (microposts with nanograss) and chemistry (coated with OTS). These experiments were performed with saturated steam (60 kPa, 86 °C) in the condensation rig with a constant surface cooling flux (160 kW m^{-2}), and the condensing droplets were photographed using a digital video camera (Nikon D300S, 24 fps) equipped with a macro lens system (Nikon 105 mm with two 2× teleconverters) and a microscope lens (Navitar 6232). We find that under identical conditions, condensation occurs first on the impregnated surface and is delayed on the unimpregnated surface (Video S5), indicating that the nucleation energy barrier is lower for impregnated surfaces, consistent with the trends reported on bulk liquids.[12] The results for droplet motion are shown in Figure 4. As seen in Figure 4a, droplets on the superhydrophobic surface were highly pinned, which was apparent by the nonspherical shape of the contact line of large droplets due to stretching by gravity (see Video S6). On the other hand, condensed droplets on the BMIm-impregnated surface moved rapidly, which is shown in Figure 4b by drawing circles around some of the droplets to show their motion. While large droplets (~1 mm) moved primarily in the direction of gravity, small ones (~100 μm) moved in random directions, creating a sweeping effect, as shown by circles and arrows in Figure 4b (see Video S6). To further characterize droplet mobility, we analyzed the motion of more than 1000 condensing droplets of various sizes on both the surfaces (see Supporting Information). We plot the speed of a representative droplet moving on the

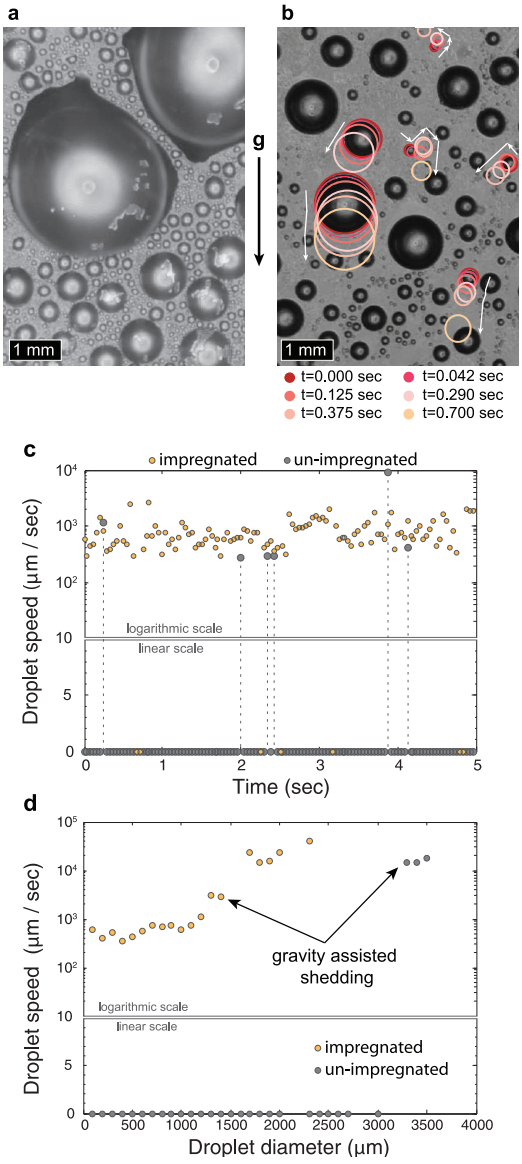

Figure 4. Comparison of condensation on hierarchical superhydrophobic and BMIm-impregnated surfaces with identical texture at macroscales. (a) Representative image of condensation on superhydrophobic surface comprising nanograss microposts; large pinned droplets are seen before shedding from the surface. (b) Representative image of condensation on nanograss microposts impregnated with BMIm. Both small and large droplets are highly mobile; colored circles are provided as a guide to eye for depicting droplet motion. (c) Speed of a representative droplet (initial diameter ~420 μm) as a function of time for unimpregnated (black circles) and impregnated surfaces (orange circles). (d) Median speed of droplets as a function of drop diameter for unimpregnated (black circles) and impregnated surfaces (orange circles). The velocities of the immobile drops that moved by less than 1 pixel were below the measurement threshold of our apparatus and, therefore, were assigned a value of zero The data are plotted on a mixed linear/logarithmic scale in order to capture both the zero value and substantial range of magnitudes in droplet speed.

BMIm-impregnated surface with time and compare it to that on the superhydrophobic surface. This is shown in Figure 4c, which shows that the droplet on the superhydrophobic surface remained mostly immobile except when it coalesced with a larger drop, resulting in a sudden increase in its speed (spikes in Figure 4c). On the other hand, the droplet on the BMIm-impregnated surface was predominantly mobile, with a speed that was several orders of magnitude higher than that on the superhydrophobic surface. Figure 4d assembles data of Figure 4c for a range of droplet sizes (from ~100 μm to gravity-induced departure) and plots their median speeds on the BMIm-impregnated and superhydrophobic surfaces. It can be seen that the median speed of droplets on the superhydrophobic surface remains negligible until the droplets grow sufficiently large to move by gravity (about 3.5 mm in diameter). In contrast, the median speed of droplets on the BMIm-impregnated surface is much higher as early as when they are 100 μm in diameter. Moreover, the median speed remains consistently high and increases even further for higher droplet sizes until they begin to shed due to gravity. These data reveal a remarkable difference between the two surfaces: while droplets on the BMIm-impregnated surface display gross continual motion, droplets on the superhydrophobic surface mostly "nudge" intermittently. The continual motion with high speeds on the BMIm-impregnated surface is extremely beneficial, as it induces a sweeping effect on the condensing surface and paves the way for nucleation of new drops. Since the condensation heat transfer is a strong function of droplet mobility,[47] we expect the BMIm-impregnated surface to exhibit superior heat transfer performance.

CONCLUSION

In summary, we show that condensation of water droplets on lubricant-impregnated nanotextured surfaces occurs with enhanced droplet mobility compared to superhydrophobic surfaces. The enhancement results from the fact that the condensed droplets stay afloat on the lubricant with minimal pinning to the surface compared with superhydrophobic surfaces, where droplets grow within textures and get strongly pinned. We describe the conditions required to ensure droplet floatation and demonstrate the effect of key parameters, such as texture geometry, surface energies of various phases, and lubricant cloaking on droplet growth and mobility. The extremely high mobility and the resultant sweeping effect of condensed drops observed on lubricant-impregnated surfaces make them promising for enhanced condensation heat transfer. The longevity of these surfaces is affected by additional factors including lubricant cloaking, drainage, and miscibility, and these durability challenges can be addressed by optimizing the texture and lubricant in future studies, as described in the Supporting Information. We identify several phenomena such as lubricant cloaking and pinning

reduction using partially wet nanotextures that are expected to have broad implications for other applications of these surfaces such as anti-icing, self-cleaning, and antifouling.

METHODS

Preparation of Square Micropost Arrays. Two centimeter square silicon substrates (n-type ⟨100⟩, 350 μm thick) were patterned *via* photolithography and etched *via* DRIE to obtain arrays of square microposts 10 μm high and 10 μm wide with 10 μm edge-to-edge spacing. The micropost arrays were further etched in a plasma of O_2 and SF_6 to obtain a nanograss texture[17,48] consisting of sharp spikes with a height of ~200 nm and a characteristic spacing of ~100 nm. After cleaning the samples with Piranha solution, they were coated with octadecyltrichlorosilane (Sigma Aldrich) using a solution deposition method, rendering the surface hydrophobic so as to allow lubricant to stably adhere to the surface in the presence of water.

Preparation of Impregnated Samples. The silanized samples were impregnated with lubricants by dipping them in a reservoir of the lubricating liquid with a dip-coater (KSV Nima multi vessel dip coater) and then carefully withdrawing at a controlled rate. Samples were withdrawn at a rate V such that the capillary number, $Ca = \mu V/\gamma$, corresponding to an impregnating lubricant with viscosity μ and surface tension γ, was less than 10^{-5}. This ensured that no excess lubricant remained on the post tops.[42]

Contact Angle Measurements. Contact angles of both lubricants on smooth OTS-coated silicon surfaces were measured in the presence of air as well as water using a Ramé-Hart model 500 Advanced goniometer. We also conducted experiments to verify that the vapor concentration does not affect the contact angle of oil on solid (see Supporting Information).

ESEM Apparatus for Microscale Condensation Observation. Environmental scanning electron microscopy was performed in a Zeiss EVO-55 and Zeiss EVO-LS10 equipped with Peltier coolers. A custom copper fixture was fabricated to mount the samples and ensure adequate thermal contact with the Peltier device. All experiments were performed under identical conditions of pressure, electron beam parameters, beam scanning rate, *etc.* The beam settings used were found to be the best optimal settings for obtaining better imaging contrast of water droplets on the lubricants, especially Krytox. Videos from ESEM experiments were analyzed using ImageJ software.[49] Droplet growth analysis was performed using methods described elsewhere.[7]

Steam Condensation Apparatus for Macroscale Condensation Observation. Sample surfaces were mounted to the face of a cylindrical copper cooling block outfitted with thermocouples to measure the cooling heat flux (Figure 5). The copper block was cooled by a water-cooled heat exchanger (NESLAB II, Thermo Scientific) and inserted into a vacuum chamber. After drawing vacuum of less than 100 Pa to remove noncondensable gas from the chamber, steam was introduced until the chamber reached a steady pressure of 60 kPa. Ultrapure saturated steam was produced by an electric boiler (SR-20, Reimers Boiler Co.) supplied with 5 MΩ deionized water passed through a nanoporous membrane degassifier (Extra-Flow, Liqui-Cel) to obtain a dissolved oxygen content of less than 1 ppm.

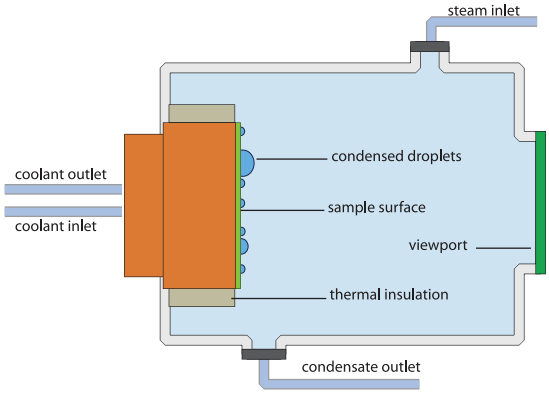

Figure 5. Schematic of steam condensation apparatus.

Conflict of Interest: The authors declare no competing financial interest.

Supporting Information Available: Spreading coefficients of Krytox and ionic liquid, effect of vapor concentration on contact angle of oil on solid, droplet mobility analysis, factors influencing lubricant lifetime, Video S1 (condensation on impregnated *vs* unimpregnated surfaces in ESEM; the video plays at 50× speed: 4 fps with time between each frame of 12.2 s), Video S2 (microscopic condensation behavior on cloaking *vs* uncloaking lubricants; the video plays at 0.5 fps; time between each frame is 2.6 s), Video S3 (ESEM video showing water does not evaporate in Krytox; the video plays at 3 fps, time between each frame is 3 s), Video S4 (ESEM video showing pinned water droplets on impregnated micropost samples compared with impregnated nanograss micropost samples; the video plays at 50× speed: 4 fps with time between each frame of 12.2 s), Video S5 (initial moments of condensation on impregnated *vs* unimpregnated surfaces; half of the surface has been impregnated with ionic liquid, while the other half remains unimpregnated; videos are both recorded and played at 24 fps), Video S6 (macroscale condensation on unimpregnated superhydrophobic nanograss microposts and impregnated nanograss micropost samples; videos are both recorded and played at 24 fps). This material is available free of charge *via* the Internet at http://pubs.acs.org.

Acknowledgment. We gratefully acknowledge support from an NSF Career Award, the Masdar-MIT Energy Initiative program, and the MIT-Deshpande Center. This work was performed in part at Harvard's Center for Nanoscale Systems and at the Forsyth Institute. We thank Prof. Paulo Lozano at MIT for providing the ionic liquid samples. We thank Adam Graham from CNS at Harvard's Center for Nanoscale Systems and Dr. Felicitas Bidlack at the Forsyth Institute for help with SEM.

REFERENCES AND NOTES

1. Rohsenow, W. M.; Hartnett, J. P.; Cho, Y. I. *Handbook of Heat Transfer*; McGraw-Hill: New York, 1998; Vol. 3, pp 12.34−12.43.
2. Carey, V. P. *Liquid-Vapor Phase-Change Phenomena*, 2nd ed.; Taylor & Francis: New York, 2007; pp 337−390.
3. Rose, J. W. Dropwise Condensation Theory and Experiment: A Review. *Proc. Inst. Mech. Eng., Part A* **2002**, *216*, 115–128.
4. Patankar, N. A. Supernucleating Surfaces for Nucleate Boiling and Dropwise Condensation Heat Transfer. *Soft Matter* **2010**, *6*, 1613–1620.
5. Beysens, D.; Knobler, C. M. Growth of Breath Figures. *Phys. Rev. Lett.* **1986**, *57*, 1433–1436.
6. Varanasi, K. K.; Hsu, M.; Bhate, N.; Yang, W.; Deng, T. Spatial Control in the Heterogeneous Nucleation of Water. *Appl. Phys. Lett.* **2009**, *95*, 094101.
7. Anand, S.; Son, S. Y. Sub-Micrometer Dropwise Condensation under Superheated and Rarefied Vapor Condition. *Langmuir* **2010**, *26*, 17100–17110.
8. Bormashenko, E.; Musin, A.; Bormashenko, Y.; Whyman, G.; Pogreb, R.; Gendelman, O. Formation of Films on Water Droplets Floating on a Polymer Solution Surface. *Macromol. Chem. Phys.* **2007**, *208*, 702–709.
9. Sokuler, M.; Auernhammer, G. K.; Roth, M.; Liu, C.; Bonacurrso, E.; Butt, H. J. The Softer the Better: Fast Condensation on Soft Surfaces. *Langmuir* **2009**, *26*, 1544–1547.
10. Knobler, C.; Beysens, D. Growth of Breath Figures on Fluid Surfaces. *Europhys. Lett.* **1988**, *6*, 707.

11. Steyer, A.; Guenoun, P.; Beysens, D. Hexatic and Fat-Fractal Structures for Water Droplets Condensing on Oil. *Phys. Rev. E* **1993**, *48*, 428–431.
12. Eslami, F.; Elliott, J. A. W. Thermodynamic Investigation of the Barrier for Heterogeneous Nucleation on a Fluid Surface in Comparison with a Rigid Surface. *J. Phys. Chem. B* **2011**, *115*, 10646–10653.
13. Umur, A.; Griffith, P. Mechanism of Dropwise Condensation. *J. Heat Transfer* **1965**, *87*, 275.
14. Mikic, B. B. On Mechanism of Dropwise Condensation. *Int. J. Heat Mass Transfer* **1969**, *12*, 1311–1323.
15. Daniel, S.; Chaudhury, M. K.; Chen, J. C. Fast Drop Movements Resulting from the Phase Change on a Gradient Surface. *Science* **2001**, *291*, 633–636.
16. Narhe, R. D.; Beysens, D. A. Nucleation and Growth on a Superhydrophobic Grooved Surface. *Phys. Rev. Lett.* **2004**, *93*, 076103.
17. Dorrer, C.; Rühe, J. Wetting of Silicon Nanograss: From Superhydrophilic to Superhydrophobic Surfaces. *Adv. Mater.* **2008**, *20*, 159–163.
18. Boreyko, J. B.; Chen, C. H. Self-Propelled Dropwise Condensate on Superhydrophobic Surfaces. *Phys. Rev. Lett.* **2009**, *103*, 184501.
19. Dorrer, C.; Rühe, J. Some Thoughts on Superhydrophobic Wetting. *Soft Matter* **2009**, *5*, 51–61.
20. Dietz, C.; Rykaczewski, K.; Fedorov, A. G.; Joshi, Y. Visualization of Droplet Departure on a Superhydrophobic Surface and Implications to Heat Transfer Enhancement During Dropwise Condensation. *Appl. Phys. Lett.* **2010**, *97*, 033104.
21. Chen, X.; Wu, J.; Ma, R.; Hua, M.; Koratkar, N.; Yao, S.; Wang, Z. Nanograssed Micropyramidal Architectures for Continuous Dropwise Condensation. *Adv. Funct. Mater.* **2011**, *21*, 4617–4623.
22. Rykaczewski, K.; Scott, J. H. J. Methodology for Imaging Nano-to-Microscale Water Condensation Dynamics on Complex Nanostructures. *ACS Nano* **2011**, *5*, 5962–5968.
23. Rykaczewski, K.; Chinn, J.; Walker, M. L.; Scott, J. H. J.; Chinn, A.; Jones, W. Dynamics of Nanoparticle Self-Assembly into Superhydrophobic Liquid Marbles during Water Condensation. *ACS Nano* **2011**, *5*, 9746–9754.
24. Miljkovic, N.; Enright, R.; Wang, E. N. Effect of Droplet Morphology on Growth Dynamics and Heat Transfer During Condensation on Superhydrophobic Nanostructured Surfaces. *ACS Nano* **2012**, *6*, 1776–1785.
25. Anderson, D. M.; Gupta, M. K.; Voevodin, A. A.; Hunter, C. N.; Putnam, S. A.; Tsukruk, V. V.; Fedorov, A. G. Using Amphiphilic Nanostructures to Enable Long-Range Ensemble Coalescence and Surface Rejuvenation in Dropwise Condensation. *ACS Nano* **2012**, *6*, 3262–3268.
26. Quéré, D. Wetting and Roughness. *Annu. Rev. Mater. Res.* **2008**; *38*, 71−99.
27. Cheng, Y. T.; Rodak, D. E. Is the Lotus Leaf Superhydrophobic? *Appl. Phys. Lett.* **2005**, *86*, 1–3.
28. Nosonovsky, M.; Bhushan, B. Biomimetic Superhydrophobic Surfaces: Multiscale Approach. *Nano Lett.* **2007**, *7*, 2633–2637.
29. Dorrer, C.; Rühe, J. Condensation and Wetting Transitions on Microstructured Ultrahydrophobic Surfaces. *Langmuir* **2007**, *23*, 3820–3824.
30. Jung, Y. C.; Bhushan, B. Wetting Behaviour during Evaporation and Condensation of Water Microdroplets on Superhydrophobic Patterned Surfaces. *J. Microsc.* **2008**, *229*, 127–140.
31. Thickett, S. C.; Neto, C.; Harris, A. T. Biomimetic Surface Coatings for Atmospheric Water Capture Prepared by Dewetting of Polymer Films. *Adv. Mater.* **2011**, *23*, 3718–3722.
32. Narhe, R. D.; González-Viñas, W.; Beysens, D. A. Water Condensation on Zinc Surfaces Treated by Chemical Bath Deposition. *Appl. Surf. Sci.* **2010**, *256*, 4930–4933.
33. He, M.; Zhou, X.; Zeng, X.; Cui, D.; Zhang, Q.; Chen, J.; Li, H.; Wang, J.; Cao, Z.; Song, Y.; Jiang, L. Hierarchically Structured Porous Aluminum Surfaces for High-Efficient Removal of Condensed Water. *Soft Matter* **2012**, *8*, 6680–6683.
34. Feng, J.; Qin, Z.; Yao, S. Factors Affecting the Spontaneous Motion of Condensate Drops on Superhydrophobic Copper Surfaces. *Langmuir* **2012**, *28*, 6067–6075.
35. Quéré, D. Non-Sticking Drops. *Rep. Prog. Phys.* **2005**, *68*, 2495–2532.
36. Lafuma, A.; Quéré, D. Slippery Pre-Suffused Surfaces. *Europhys. Lett.* **2011**, *96*, 56001.
37. Wong, T. S.; Kang, S. H.; Tang, S. K. Y.; Smythe, E. J.; Hatton, B. D.; Grinthal, A.; Aizenberg, J. Bioinspired Self-Repairing Slippery Surfaces with Pressure-Stable Omniphobicity. *Nature* **2011**, *477*, 443–447.
38. Kim, P.; Wong, T.-S.; Alvarenga, J.; Kreder, M. J.; Adorno-Martinez, W. E.; Aizenberg, J. Liquid-Infused Nanostructured Surfaces with Extreme Anti-Ice and Anti-Frost Performance. *ACS Nano* **2012**, *6*, 6569–6577.
39. Smith, J. D.; Dhiman, R.; Varanasi, K. K. Liquid-Encapsulating Surfaces: Overcoming the Limitations of Superhydrophobic Surfaces for Robust Non-Wetting and Anti-Icing Surfaces. *Bull. Am. Phys. Soc.* **2011**, 56.
40. Harkins, W. D.; Feldman, A. Films. The Spreading of Liquids and the Spreading Coefficient. *J. Am. Chem. Soc.* **1922**, *44*, 2665–2685.
41. De Gennes, P. G.; Brochard-Wyart, F.; Quéré, D. *Capillarity and Wetting Phenomena: Drops, Bubbles, Pearls, Waves*; Springer Verlag: 2004; pp 54−56.
42. Seiwert, J.; Clanet, C.; Quéré, D. Coating of a Textured Solid. *J. Fluid Mech.* **2011**, *669*, 55–63.
43. Stauffer, C. E. The Measurement of Surface Tension by the Pendant Drop Technique. *J. Phys. Chem.* **1965**, *69*, 1933–1938.
44. Freire, M. G.; Carvalho, P. J.; Fernandes, A. M.; Marrucho, I. M.; Queimada, A. J.; Coutinho, J. A. P. Surface Tensions of Imidazolium Based Ionic Liquids: Anion, Cation, Temperature and Water Effect. *J. Colloid Interface Sci.* **2007**, *314*, 621–630.
45. Jacquemin, J.; Husson, P.; Padua, A.; Majer, V. Density and Viscosity of Several Pure and Water-Saturated Ionic Liquids. *Green Chem.* **2006**, *8*, 172–180.
46. Steyer, A.; Guenoun, P.; Beysens, D.; Knobler, C. M. Two-Dimensional Ordering during Droplet Growth on a Liquid Surface. *Phys. Rev. B* **1990**, *42*, 1086–1089.
47. Rose, J. W.; Glicksman, L. R. Dropwise Condensation-The Distribution of Drop Sizes. *Int. J. Heat Mass Transfer* **1973**, *16*, 411–425.
48. Jansen, H.; Boer, M.; Legtenberg, R.; Elwenspoek, M. The Black Silicon Method: a Universal Method for Determining the Parameter Setting of a Fluorine-Based Reactive Ion Etcher in Deep Silicon Trench Etching with Profile Control. *J. Micromech. Microeng.* **1995**, *5*, 115.
49. Abràmoff, M. D.; Magalhães, P. J.; Ram, S. J. Image Processing with ImageJ. *Biophotonics Int.* **2004**, *11*, 36–41.